

DiffDA: a Diffusion model for weather-scale Data Assimilation

Langwen Huang¹ Lukas Gianinazzi¹ Yuejiang Yu¹ Peter D. Dueben² Torsten Hoefler¹

Abstract

The generation of initial conditions via accurate data assimilation is crucial for weather forecasting and climate modeling. We propose DiffDA as a denoising diffusion model capable of assimilating atmospheric variables using predicted states and sparse observations. Acknowledging the similarity between a weather forecast model and a denoising diffusion model dedicated to weather applications, we adapt the pretrained GraphCast neural network as the backbone of the diffusion model. Through experiments based on simulated observations from the ERA5 reanalysis dataset, our method can produce assimilated global atmospheric data consistent with observations at 0.25° ($\approx 30\text{km}$) resolution globally. This marks the highest resolution achieved by ML data assimilation models. The experiments also show that the initial conditions assimilated from sparse observations (less than 0.77% of gridded data) and 48-hour forecast can be used for forecast models with a loss of lead time of at most 24 hours compared to initial conditions from state-of-the-art data assimilation in ERA5. This enables the application of the method to real-world applications, such as creating reanalysis datasets with autoregressive data assimilation.

1. Introduction

Weather forecast plays an important role in our daily life. Due to uncertainties in the weather forecast process, the predicted weather will inevitably deviate from the actual weather. It is necessary to “pull-back” the predicted weather state via *data assimilation*, making it consistent with observations from weather stations and satellites. Practically, as [Figure 1](#) shows, the data assimilation process generates initial conditions of weather simulation models from predicted

^{*}Equal contribution ¹Department of Computer Science, ETH Zürich, Switzerland ²European Centre for Medium-Range Weather Forecasts (ECMWF), Reading, United Kingdom. Correspondence to: Langwen Huang <langwen.huang@inf.ethz.ch>, Torsten Hoefler <torsten.hoefler@inf.ethz.ch>.

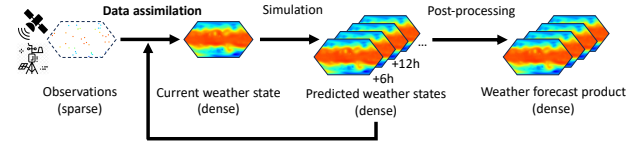


Figure 1. Diagram of numerical weather forecast pipeline. It consists of data assimilation, simulation and post-processing. Data assimilation produces gridded values from sparse observations and predicted gridded values from previous time steps. Simulation takes in gridded values and produces predictions in gridded values at future time steps. Post-processing improves prediction so that it is closer to future observations.

weather state and sparse observations made at different locations. The quality of these weather simulation models depends heavily on the data assimilation since errors in initial conditions are one of the main sources for errors in weather forecasts ([Bonavita et al., 2016](#)). Additionally, data assimilation is employed in creating reanalysis datasets, which contain reconstructed historical weather variables as gridded fields. These reanalysis datasets play a central role in weather and climate research ([ipc, 2023](#); [Hersbach et al., 2020](#)), and are essential for the training of ML weather forecast models ([Pathak et al., 2022](#); [Bi et al., 2023](#); [Lam et al., 2023](#)).

Various data assimilation methods have been developed and employed to address different characteristics of observation data and system dynamics. Among those, variational data assimilation and ensemble Kalman filter are the two most applied families of methods in operational data assimilation ([Bannister, 2017](#)). The variational method solves an optimization problem by minimizing a cost function that measures the discrepancy between simulations and observations. It requires multiple iterations in which linearized observations and evolution functions are evaluated to compute the gradient of the cost function. The linearized observation and evolution function have to be implemented separately. This adds extra overheads because the linearized functions have similar complexity as the original function, and a lot of effort has to be invested in maintaining the consistency of the original and linearized code. The ensemble Kalman filter method updates the state estimation according to the covariance matrix calculated from ensemble simulations.

DiffDA: a Diffusion model for weather-scale Data Assimilation

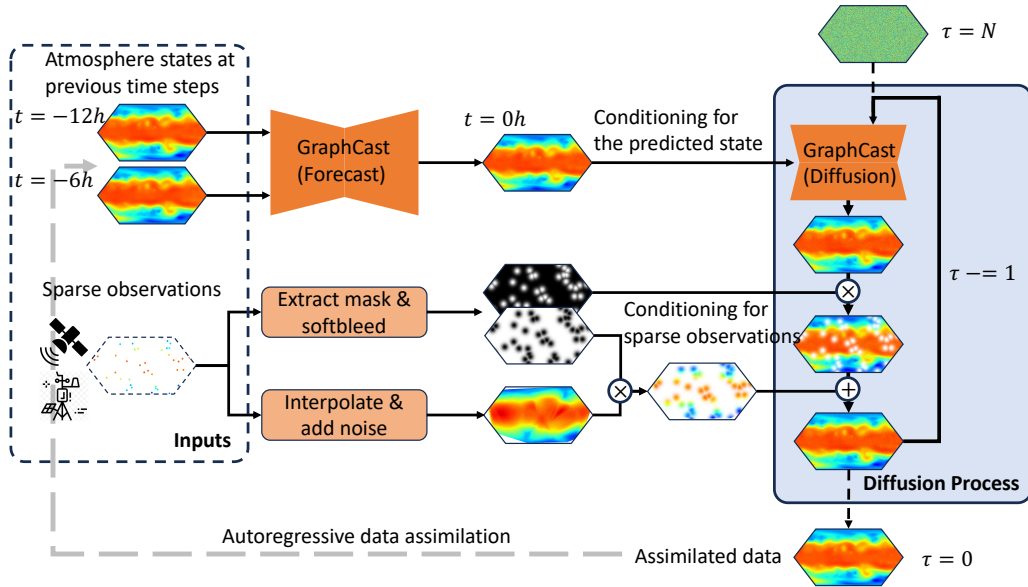


Figure 2. Architecture of the diffusion-based data assimilation method. We take advantage of the input and output shape of the pretrained GraphCast model, which takes the state of the atmosphere at two time steps as input. In each iteration of the denoising diffusion process, the adapted GraphCast model takes the predicted state and the assimilated state with noise, and further denoises the assimilated state. To enforce the observation values at inference time, The denoised state is merged with interpolated observations using a soft mask created by softbleeding the hard mask derived from the original observations.

Both approaches are computationally intensive as one requires multiple optimization iterations and the other requires multiple ensemble simulations.

Data assimilation tools are becoming a bottleneck in the simulation pipeline. While traditional data assimilation methods are sufficiently competent in operational weather forecasts (Bonavita et al., 2016), their high costs restrict broader adoptions, making them tightly coupled with a specific numerical weather forecast model. This restriction becomes more evident since the explosion of ML weather forecast models (Pathak et al., 2022; Lam et al., 2023; Bi et al., 2023). Those models claim to be a replacement of the traditional models by achieving competitive or even superior accuracy compared to the best operational model while being orders of magnitude faster. Ironically, they cannot independently make forecasts as they are all trained and evaluated on the ERA5 dataset (Hersbach et al., 2020) which is produced by the traditional data assimilation method together with the numerical forecast model.

In a probabilistic view, data assimilation can be formulated as sampling from a probability distribution of atmosphere states conditioned on observations and predicted states (Law et al., 2015; Evensen et al., 2022). Capable of solving this conditional sampling problem, denoising diffusion models (Ho et al., 2020) naturally become a tentative choice for data assimilation. Moreover, the blooming community of diffusion models provides an arsenal of techniques for

enforcing conditions of different kinds. In particular, conditioning techniques for in-painting (Lugmayr et al., 2022; Song et al., 2020) and super-resolution (Saharia et al., 2022; Chung et al., 2022) are of special interest, because they are similar to conditioning of observations and predicted states respectively. This denoising diffusion model approach has been applied in relatively small-scale data assimilation problems (Rozet and Louppe, 2023a;b; Finn et al., 2023; Andry et al., 2023), but none of them can assimilate data with a resolution comparable with the ERA5 dataset (0.25° horizontal resolution) thus limiting their use with ML forecast models. Similarly, the denoising diffusion techniques have been applied in weather forecasts (Price et al., 2023) and post-processing (Mardani et al., 2023; 2024; Li et al., 2023) with either limited resolution or limited region. While not using diffusion techniques, MetNet3 (Andrychowicz et al., 2023) can make regional weather forecasts from gridded weather data and sparse observations. It combines data assimilation with prediction into one end-to-end process.

In this work, we propose a new approach to data assimilation based on the denoising diffusion model with a focus on weather and climate applications. We are able to scale to 0.25° horizontal resolution with 13 vertical levels by utilizing an established ML forecast model GraphCast (Lam et al., 2023) as the backbone of the diffusion model. As we do not have real-world observations available from the ERA5 dataset, we are using grid columns of the ERA5 re-analysis dataset as proxies for observations. During training,

the diffusion model is conditioned with the predicted state – meaning the atmospheric state produced by the forecast model from earlier initial conditions. During inference, we further condition the model with sparse column observations following Repaint (Lugmayr et al., 2022). In addition, we use a soft mask and interpolated observations to strengthen the conditioning utilizing the continuity of atmospheric variables. The resulting assimilated data can converge to the ground truth field when the number of simulated observation columns increases. More importantly, the assimilated data can be used as the input of the forecast model at a loss of lead time not exceeding 24 hours. We also test the autoregressive data assimilation to generate a reanalysis dataset given a series of observations and an initial predicted field.

Our key contributions are:

1. We demonstrate a novel ML data assimilation method capable of assimilating high resolution data. The assimilated data is ready for weather forecast applications.
2. We are able to create data assimilation cycles combining our method and an ML forecast model. The resulting reanalysis dataset is consistent with the given observation.
3. We build our method using a neural network backbone from a trained ML forecast model. It is easy to upgrade the backbone with any state-of-the-art model due to the flexibility of our method.

2. Method

2.1. Problem formulation

The goal of data assimilation is to reconstruct atmospheric variables on a fixed grid with n grid points $\mathbf{x}_i \in \mathbb{R}^n$ at physical time step i given m measurements $\mathbf{y}_i = f(\mathbf{x}_i^*), \mathbf{y}_i \in \mathbb{R}^m, \mathbf{x}_i^* \in \mathbb{R}^n$ where \mathbf{x}_i^* is the ground truth of atmospheric variables on grid points at time step i . In addition, estimated values on grid points $\hat{\mathbf{x}}_i = \mathcal{F}(\mathbf{x}_{i-1})$ produced by the forecast model $\mathcal{F} : \mathbb{R}^n \rightarrow \mathbb{R}^n$ are also provided as the inputs. In a probabilistic view, data assimilation samples from a conditional distribution $p(\mathbf{x}_i | \hat{\mathbf{x}}_i, \mathbf{y}_i)$ which minimizes the discrepancy between \mathbf{x}_i and \mathbf{x}_i^* . To simplify the problem, f is limited to a sparse linear observation operator $\mathbf{y}_i = f(\mathbf{x}_i^*) = \mathbf{A}\mathbf{x}_i^*$ where \mathbf{A} is a sparse matrix with only one nonzero value in each row. In real-world cases, this simplification applies to point observations such as temperature, pressure, and wind speed measurements at weather stations and balloons.

2.2. Denoising diffusion probabilistic model

The denoising diffusion probabilistic model (DDPM) is a generative model capable of sampling from the probabilistic

distribution defined by the training data (Ho et al., 2020). It is trained to approximate the reverse of the diffusion process where noise is added to a state vector \mathbf{x}^0 during N diffusion steps, resulting in an isotropic Gaussian noise vector $\mathbf{x}^N \sim \mathcal{N}(\mathbf{0}, \mathbf{I})$. We denote the state vector at physical time step i and diffusion step j with \mathbf{x}_i^j . We write \mathbf{x}^j whenever the statement is independent of the physical time step. Note that the diffusion step j and the physical time step i are completely independent of each other.

For each diffusion step j , the diffusion process can be seen as sampling from a Gaussian distribution with a mean of $\sqrt{1 - \beta_j}\mathbf{x}^{j-1}$ and covariance matrix of $\beta_j\mathbf{I}$:

$$p(\mathbf{x}^j | \mathbf{x}^{j-1}) = \mathcal{N}(\sqrt{1 - \beta_j}\mathbf{x}^{j-1}, \beta_j\mathbf{I}) \quad (1)$$

where $\beta_j > 0$ is the variance schedule.

A denoising diffusion model μ_θ is used to predict the mean of \mathbf{x}^{j-1} given \mathbf{x}^j and j with the following parameterization:

$$\mu_\theta(\mathbf{x}^j, j) = \frac{1}{\sqrt{1 - \beta_j}} \left(\mathbf{x}^j - \frac{\beta_j}{\sqrt{1 - \bar{\alpha}_j}} \epsilon_\theta(\mathbf{x}^j, j) \right) \quad (2)$$

where θ are the trainable parameters, $\bar{\alpha}_j = \prod_{s=1}^j (1 - \beta_s)$. Then, \mathbf{x}^{j-1} can be sampled from $p(\mathbf{x}^{j-1} | \mathbf{x}^j) = \mathcal{N}(\mu_\theta(\mathbf{x}^j, j), \frac{1 - \bar{\alpha}_{j-1}}{1 - \bar{\alpha}_j} \beta_j \mathbf{I})$ to reverse the diffusion process. Applying this procedure N times from $\mathbf{x}^N \sim \mathcal{N}(\mathbf{0}, \mathbf{I})$, we can generate \mathbf{x}^0 which follows a similar distribution as the empirical distribution of the training data.

During the training phase, we minimize the following loss function:

$$L(\theta) = \mathbb{E}_{j \sim U[1, N], \mathbf{x}^{0*} \sim \text{training data}, \epsilon \sim \mathcal{N}(\mathbf{0}, \mathbf{I})} [\|\epsilon - \epsilon_\theta(\mathbf{x}^j, j)\|^2]. \quad (3)$$

\mathbf{x}^j can be expressed in a closed form: $\mathbf{x}^j = \sqrt{\bar{\alpha}_j}\mathbf{x}^{0*} + \sqrt{(1 - \bar{\alpha}_j)}\epsilon$ because the diffusion process applies independent Gaussian noise at each step, and thus $p(\mathbf{x}^j | \mathbf{x}^{0*}) = \mathcal{N}(\sqrt{\bar{\alpha}_j}\mathbf{x}^{0*}, (1 - \bar{\alpha}_j)\mathbf{I})$.

With the unconditional denoising diffusion model above, we add the conditioning of predicted state $\hat{\mathbf{x}}$ and observation \mathbf{y} separately according to their characteristics.

2.3. Conditioning for predicted state

Utilizing the fact that the predicted state $\hat{\mathbf{x}}$ has the same shape as the diffused state \mathbf{x}^j , it is convenient to add the predicted state as an additional input for the (reparameterized) diffusion model denoted as $\epsilon_\theta(\mathbf{x}^j, \hat{\mathbf{x}}, j)$ (Saharia et al., 2022). The underlying neural network can concatenate \mathbf{x}^j and $\hat{\mathbf{x}}$ in their feature channels without changing its architecture as shown in Figure 2.

Since ϵ_θ (and μ_θ) is dependent on $\hat{\mathbf{x}}$, the reverse diffusion process becomes sampling from $p(\mathbf{x}^{j-1} | \mathbf{x}^j, \hat{\mathbf{x}}) =$

$\mathcal{N}(\mu_\theta(\mathbf{x}^j, \hat{\mathbf{x}}, j), \frac{1-\bar{\alpha}_{j-1}}{1-\bar{\alpha}_j}\beta_j\mathbf{I})$. Therefore, the generated \mathbf{x}^0 is sampled from the conditional distribution $p(\mathbf{x}^0|\hat{\mathbf{x}}) = p(\mathbf{x}^N) \prod_{j=1}^N p(\mathbf{x}^{j-1}|\mathbf{x}^j, \hat{\mathbf{x}})$.

This method requires sampling pairs of \mathbf{x}^{0*} and $\hat{\mathbf{x}}$ during training. This can be realized by sampling two states $\mathbf{x}_{i-1}^*, \mathbf{x}_i^*$ with consecutive physical time steps from training data, and then apply the forecast model to get the predicted state at physical time i : $\hat{\mathbf{x}}_i = \mathcal{F}(\mathbf{x}_{i-1}^*)$. Afterwards, the sampled (ground truth) state \mathbf{x}_i^* is diffused with random $j \in [1, N]$ steps which is implemented with the closed form formula: $\mathbf{x}_i^j = \sqrt{\bar{\alpha}_j}\mathbf{x}_i^{0*} + \sqrt{(1-\bar{\alpha}_j)}\epsilon$, $\epsilon \sim \mathcal{N}(\mathbf{0}, \mathbf{I})$. Finally, we can take one gradient step based on $\nabla_\theta \|\epsilon - \epsilon_\theta(\mathbf{x}_i^j, \hat{\mathbf{x}}_i, j)\|^2$ to train the diffusion model.

With the conditioning of the predicted state alone, we can already perform backward diffusion steps using the trained model μ_θ which results in $\mathbf{x}^0 \sim p(\mathbf{x}^0|\hat{\mathbf{x}})$. This means we corrected, or in other words, ‘‘post-processed’’ the predictions $\hat{\mathbf{x}}$ to be closer to the ground truth state \mathbf{x}^* .

2.4. Conditioning for sparse observations

The conditioning for sparse observations poses a different challenge than the conditioning on the predicted state. The sparse observations \mathbf{y} have a variable length m as opposed to a fixed length n , and the data assimilation results are invariant to the permutation of the m elements in \mathbf{y} . This requires dedicated design in the neural network if we want to directly condition μ_θ with \mathbf{y} as before. Even if we find a solution to implement that, the trained diffusion model will have an generalization problem because the possible input space spanned by \mathbf{x}^0 , $\hat{\mathbf{x}}$, and \mathbf{y} is too large and hard to thoroughly sample during training.

To avoid those issues, we follow inpainting techniques (Lugmayr et al., 2022; Song et al., 2020) to enforce the conditioning of observations at inference time. Let us start with a simple approach first. It creates a hard mask $\mathbf{m}_h \in \{0, 1\}^n$ to indicate which grid columns of the atmospheric state are observed, where a 1 means the associated value in \mathbf{x}^* is observed in \mathbf{y} and vice versa. The mask equals the sum of the columns of the observation matrix $\mathbf{A} \in \mathbb{R}^{n \times m}$ where $\mathbf{y} = \mathbf{A}\mathbf{x}^*$. During the inference of the diffusion model, a state vector with white Gaussian noise is created and gradually denoised by the denoising diffusion model. However, with \mathbf{y} present, we have better knowledge of the observed locations in the state vector: values can be produced by a forward diffusion process from the observation data. We can use the mask \mathbf{m}_h to treat the two parts separately and combine them in each iteration of the denoising process

(Figure 2).

$$\begin{aligned} \mathbf{x}_{\text{known}}^{j-1} &\sim \mathcal{N}(\sqrt{\bar{\alpha}^{j-1}}\mathbf{x}^*, (1-\bar{\alpha}^{j-1})\mathbf{I}) \\ \mathbf{x}_{\text{unknown}}^{j-1} &\sim \mathcal{N}(\mu_\theta(\mathbf{x}^j, j), \frac{1-\bar{\alpha}_{j-1}}{1-\bar{\alpha}_j}\beta_t\mathbf{I}) \\ \mathbf{x}^{j-1} &= \mathbf{m}_h \odot \mathbf{x}_{\text{known}}^{j-1} + (1-\mathbf{m}_h) \odot \mathbf{x}_{\text{unknown}}^{j-1} \end{aligned}$$

Here, \odot denotes point-wise multiplication used to filter observed and non-observed values. Although this method can guide diffusion results to the observed values, it performs poorly in practice because only the values at the observation locations are forced to the given values while other values remain unchanged as in the unconditional scenario. This likely relates to the encoding-process-decoding architecture commonly used in diffusion models: the encoding and decoding layers employ pooling to downscale and upscale in spatial dimensions. While it helps to condense information and reduce calculations, it also smears out local details. As a result, the added conditioning information is often lost during this process.

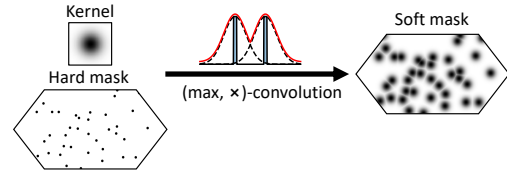


Figure 3. Creating a soft mask from a hard mask using softbleed. Softbleed performs a (max, \times)-convolution over the Gaussian kernel and the hard mask.

We tackle this issue using a ‘‘soft mixing’’ instead of a hard one. In the soft mixing, we replace the hard mask \mathbf{m}_h with a soft mask \mathbf{m}_s by applying softbleeding to \mathbf{m}_h (Figure 3) with standard deviation σ_G (for Gaussian kernel), and diameter d . The softbleed process mimics the Gaussian blurring but replaces the convolution with the (max, \times)-convolution to ensure those 1-valued points in the hard mask remain the same in the soft mask. The support region of \mathbf{m}_s (where its values are larger than 0) is larger than the support region of the observed values. As the atmospheric variables are relatively continuous over space, we interpolate the observed values to fill the support region of \mathbf{m}_s . There is abundant flexibility in choosing interpolation algorithms. We use the linear interpolation algorithm provided in SCIPY package (Virtanen et al., 2020). In summary, the inference iteration becomes:

$$\begin{aligned} \mathbf{m}_s &= \text{Softbleed}(\mathbf{m}_h, \sigma_G, d) \\ \mathbf{x}^{*'} &= \text{Interpolate}(\mathbf{m}_h \odot \mathbf{x}^*, d) \\ \mathbf{x}_{\text{known}}^{j-1} &\sim \mathcal{N}(\sqrt{\bar{\alpha}^{j-1}}\mathbf{x}^{*'}, (1-\bar{\alpha}^{j-1})\mathbf{I}) \\ \mathbf{x}_{\text{unknown}}^{j-1} &\sim \mathcal{N}(\mu_\theta(\mathbf{x}^j, j), \frac{1-\bar{\alpha}_{j-1}}{1-\bar{\alpha}_j}\beta_t\mathbf{I}) \\ \mathbf{x}^{j-1} &= \mathbf{m}_s \odot \mathbf{x}_{\text{known}}^{j-1} + (1-\mathbf{m}_s) \odot \mathbf{x}_{\text{unknown}}^{j-1}. \end{aligned} \tag{4}$$

In addition, we also applied the resampling technique from (Lugmayr et al., 2022) to further reduce the inconsistency between the known part and unknown part. For each denoising iteration, the resampling technique repeats the iteration U times by pulling the resulting \mathbf{x}^{j-1} back to \mathbf{x}^j with the forward diffusion process (1) and repeating the denoising step (4). The overall algorithm of applying the denoising diffusion model for data assimilation is presented in Algorithm 1.

Algorithm 1 Data assimilation (inference)

Input: predicted state $\hat{\mathbf{x}}$, hard mask of observations \mathbf{m}_h , observation values at grid points $\mathbf{m}_h \odot \mathbf{x}^*$ (created from observation vector \mathbf{y} , and observation operator \mathbf{A}), covariance schedule $\beta_j, j = 1, \dots, N$, Gaussian kernel standard deviation σ_G , Gaussian kernel diameter d , scaling factor s

Output: $\mathbf{x} \sim p(\mathbf{x}|\hat{\mathbf{x}}, \mathbf{y})$

$\mathbf{m}_s = \text{Softbleed}(\mathbf{m}_h, \sigma_G, d)$

$\mathbf{x}^{*'} = \text{Interpolate}(\mathbf{m}_h \odot \mathbf{x}^*, d)$

$\mathbf{x}^N \sim \mathcal{N}(\mathbf{0}, \mathbf{I})$

for j in $N, \dots, 1$ **do**

CONDITIONING FOR PREDICTED STATE

$$\bar{\alpha}_j = \prod_{s=1}^j (1 - \beta_s)$$

$$\bar{\mathbf{x}}_{\text{unknown}}^{j-1} = \frac{1}{\sqrt{1-\beta_j}} \left(\mathbf{x}^j - \frac{\beta_j}{\sqrt{1-\bar{\alpha}_j}} \epsilon_{\theta}(\mathbf{x}^j, \hat{\mathbf{x}}, j) \right)$$

$$\mathbf{x}_{\text{unknown}}^{j-1} \sim \mathcal{N}(\bar{\mathbf{x}}_{\text{unknown}}^{j-1}, \frac{1-\bar{\alpha}_{j-1}}{1-\bar{\alpha}_j} \beta_j \mathbf{I})$$

CONDITIONING FOR SPARSE OBSERVATIONS

$$\mathbf{x}_{\text{known}}^{j-1} \sim \mathcal{N}(\sqrt{\bar{\alpha}^{j-1}} \mathbf{x}^{*'}, (1 - \bar{\alpha}^{j-1}) \mathbf{I})$$

$$\mathbf{x}^{j-1} = \mathbf{m}_s \odot \mathbf{x}_{\text{known}}^{j-1} + (1 - \mathbf{m}_s) \odot \mathbf{x}_{\text{unknown}}^{j-1}$$

end for

$\mathbf{x} = \hat{\mathbf{x}} + s \odot \mathbf{x}^0$ (apply skip connection)

2.5. Selection of diffusion model structure

Our method provides a lot of flexibility on the selection of the neural network structure for $\epsilon_{\theta}(\mathbf{x}_i^j, \hat{\mathbf{x}}_i, j) : \mathbb{R}^n \times \mathbb{R}^n \times \mathbb{N}^+ \rightarrow \mathbb{R}^n$ as any neural network that matches the function signature will work. However, n can be tens of millions in practice, rendering many neural network architectures infeasible due to resource constraints. A neural network must utilize the spatial information in the state vector \mathbf{x} to learn efficiently.

Instead of creating a new architecture, we employ a proven architecture in ML weather forecast models. It has a similar signature $\mathbb{R}^{c \cdot n} \rightarrow \mathbb{R}^n, c \in \mathbb{N}^+$ as the diffusion model. Due to this similarity, neural networks that perform well in forecasting should also do well in the data assimilation tasks, and it is likely to take fewer training steps using pre-trained weights of the forecast model when training the diffusion model. Moreover, we can easily update the backbone of the diffusion model with the state-of-the-art weather forecast model.

3. Experiments

3.1. Implementation

We demonstrate our method in a real-world scenario containing 6 pressure-level variables and 4 surface variables, with a horizontal resolution of 0.25° and 13 vertical levels. This matches the resolution of the WeatherBench2 dataset (Rasp et al., 2023) used by state-of-the-art ML weather forecast models. We use the GraphCast model as the backbone of the diffusion model because the pretrained model takes in states at two consecutive time steps $\mathbf{x}_{i-1}, \mathbf{x}_i$ to predict \mathbf{x}_{i+1} . It takes much less effort than other forecast models to re-purpose it to $\epsilon_{\theta}(\mathbf{x}_i^j, \hat{\mathbf{x}}_i, j)$ given that there is one-to-one matching between \mathbf{x}_{i-1} and \mathbf{x}_i^j , as well as \mathbf{x}_{i+1} and $\hat{\mathbf{x}}_i$. As is determined by the pre-trained GraphCast model, the input size n is set to $(6 \times 13 + 4) \times 721 \times 1440$.

The diffusion model is implemented with the JAX library (Bradbury et al., 2018), DIFFUSERS library (von Platen et al., 2023), and the official implementation of GraphCast. We use the AdamW optimizer (Loshchilov and Hutter, 2018) with a warm-up cosine annealing learning rate schedule that starts from 10^{-5} , peaks at 10^{-4} after 1/6 of total training steps, and ends at 3×10^{-6} . We perform data-parallel training on 48 NVIDIA A100 GPUs with a (global) batch size of 48 for 20 epochs. Gradient checkpoints are added in the GraphCast model to reduce the GPU memory footprint. The training takes approximately 2 days. All the inference is performed on a single node with one A100 GPU, which produces an assimilated state in around 15 minutes.

3.2. Training data

We use the WeatherBench2 dataset as the first part of the training data. The dataset contains values for our target atmospheric variables from 1979 to 2016 with a time interval of 6 hours extracted from the ERA5 reanalysis dataset. Data from 1979 to 2015 is used for training, while the rest is used for validation and testing. The second part of the training data is generated by running 48-hour GraphCast predictions (with 8 time steps) using the data from the first part as initial conditions. Then, the two parts are paired up according to their physical time. Before feeding it to the model, the input data is normalized using the vertical-level-wise means and standard deviations provided by the pre-trained GraphCast model. The output of the model is de-normalized using the same means and standard deviations. Since the predicted state $\hat{\mathbf{x}}$ is close to the ground truth \mathbf{x}^* , we add a skip connection from $\hat{\mathbf{x}}$ to the de-normalized model output and use the normalized difference $\mathbf{x}_i^{0*} - \hat{\mathbf{x}}, \hat{\mathbf{x}}$ as the actual input data to the diffusion model. Following GraphCast, the normalization and de-normalization use different sets of means and standard deviations for original data $\hat{\mathbf{x}}$ and delta data $\mathbf{x}_i^{0*} - \hat{\mathbf{x}}$.

3.3. Treatment of conditioning for sparse observations

Acknowledging the multidimensional nature of the state vector and that most meteorological observations are co-located horizontally (longitude and latitude), we opt for a simplified setting in the conditioning of sparse observations. In this scenario, the observational data is m sampled columns of the ground truth state vector with $6 \times 13 + 4$ values in each column: $\mathbf{y} \in \mathbb{R}^{(6 \times 13 + 4) \times m}$. The mask is simplified to a 2D mask $\mathbf{m}_s \in \mathbb{R}^{721 \times 1440}$ which is broadcast to other dimensions when doing point-wise multiplication with the state vector in Equation (4). Interpolation is also applied independently over 2D horizontal slices for each variable and level. To interpolate appropriately for values on a sphere, we project the 2D slice into 3D space on a unit sphere and use the unstructured interpolation function GRIDDATA from the SCIPY package (Virtanen et al., 2020).

3.4. Experiment settings and results

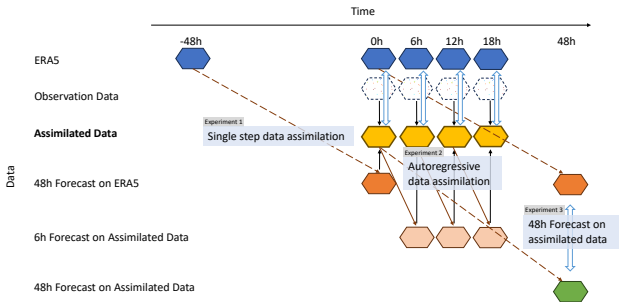


Figure 4. Overview of the experiment settings. Hexagons represent atmosphere states, black arrows represent data assimilation, brown solid arrows represent 6-hour prediction, brown dashed arrows represent 48-hour prediction, hexagons with dashed edges and sparse points represent sparse observations, and wide arrows point out targets and references to compare in each experiment.

We demonstrate the effectiveness of our method by performing real-world inspired experiments with increasing complexity (Figure 4). In the basic scenario, we perform data assimilation on 48-hour forecast and observation data, then directly compare the assimilated data with the ground truth. Furthermore, we evaluate our method with autoregressive data assimilation, where the predicted state is produced by a 6-hour prediction from the assimilated state 6 hours ago. We designed this experiment to test whether the assimilated data will deviate from the ground truth data, which is crucial in real-world applications. We also designed another experiment to compare the 48-hour forecast based on assimilated data and ground truth data and evaluate the effect of the data assimilation method on the forecast skill. For single-step data assimilation and forecast on single-step data assimilation, we run 16 parallel experiments with different inputs

and random seeds and present the result in average values. For the autoregressive data assimilation, we run each experiment once due to the limitations of computation resources. In all the experiments, observations are simulated by taking random columns from the ERA5 dataset considered as the ground truth. We vary the number of observed columns m in the experiments to test the convergence property of our data assimilation method.

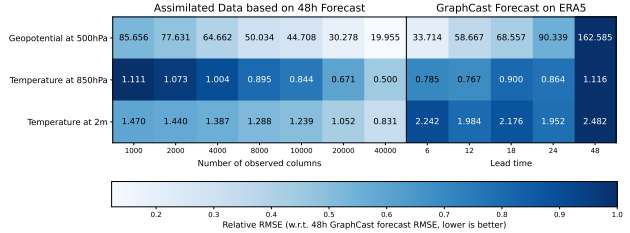


Figure 5. Root mean square errors (RMSEs, shown by the numbers in the cell) of geopotential at 500hPa, temperature at 850hPa, and temperature at 2m from the single-step assimilated data, and from 6-hour to 48-hour GraphCast forecasts. The errors are calculated against the ERA5 data. The cells are color-coded with the RMSEs relative to the 48-hour forecast errors.

Single-step data assimilation In this experiment, we perform data assimilation from a 48-hour prediction using GraphCast and columns of observations ranging from 1,000 to 40,000, then calculate the error between the assimilated data and the ERA5 data. Finally, we compare this error against GraphCast forecast errors with 6-hour to 48-hour lead times.

The result is presented in Figure 5 where we pick three representative variables closely related to forecast skills (Ashkboos et al., 2022; Rasp et al., 2020) including geopotential at 500hPa (z_{500}), temperature at 850hPa (t_{850}), and temperature at 2m (t_{2m}) as the target variables. More results can be found in subsection A.2. With only 1,000 observed columns ($< 0.1\%$ total columns), the assimilated data achieves lower RMSEs than the input 48-hour forecast for z_{500} and t_{850} . At the same time, the errors of t_{2m} are even lower than the 6-hour forecast. The errors further decrease as the number of observed columns increases. On the other side of the spectra, with 40,000 observed columns ($< 3.9\%$ total columns), the RMSEs of all three variables are lower than the 6-hour forecast error. This indicates our assimilation method can improve over the given predicted state while remaining consistent with the observations.

Autoregressive data assimilation In an operational data assimilation system, data assimilation is performed in an autoregressive way: assimilated data from previous time steps are used for producing forecast at the next time step,

which is in turn used for assimilating data at that time step. Following this setting, we perform an autoregressive data assimilation cycle: it starts from a 48-hour forecast at 0 hour, and repeats the data assimilation - 6-hour forecast cycle autoregressively. We train two separate diffusion models for this task, one dedicated to 48-hour forecast inputs and the other dedicated to 6-hour forecast inputs. In the data assimilation cycle, two strategies of sampling the simulated observation columns are used. One is to sample the columns at the same locations (Figure 6). The other resamples data at different locations in each iteration (Figure 7). The strategies help estimate the performance in real-world cases since the reality is the mix of the two strategies where some observations are measured at the same locations, such as weather stations and geostationary satellites, while locations of other observations change with time. We evaluate the autoregressive data assimilation result similar to the previous experiment.

We observe distinct patterns for fixed and non-fixed sampling strategies in the results. With fixed sampling (Figure 6), the initial five iterations show promising performance, but errors begin to accumulate in subsequent iterations. The assimilated data with 1,000 columns of observations ($< 0.1\%$ total columns) quickly diverts from the ERA5 data especially for the z_{500} variable, but this is not the case with more observations. It implies that the given observations are not sufficient to balance the error accumulation in the forecast model. In contrast, the non-fixed sampling strategy shows a slower error accumulation rate than fixed sampling (Figure 7). However, an issue is identified in both strategies: the assimilated errors (solid lines) consistently exceed the interpolation errors (dashed lines) after several iterations. This is less of a concern in real-world scenarios where lots of the observations, such as satellite imagery and radar soundings, can not be explicitly interpolated into atmospheric variables. Notably, the assimilation errors of t_{2m} indicate a diurnal pattern with a period of 24 hours. Since the interpolation errors remain stable over iterations, this diurnal pattern is likely introduced by the GraphCast forecast model.

Forecast on single-step assimilated data Since assimilated data is often used as the input of weather forecasts, it is important to test the forecast error using our assimilated data. In this experiment, we perform data assimilation at 0 hour, perform a 48-hour prediction using GraphCast, and then compare the resulting errors against the forecast errors with varying lead times using ERA5 at 0 hour as inputs.

As the scoreboard plot in Figure 8 shows, results from this experiment reveal that the 48-hour forecast errors using assimilated data inputs gradually converge to the 48-hour forecast errors using ERA5 inputs. More results can be found in subsection A.3. The errors using assimilated data

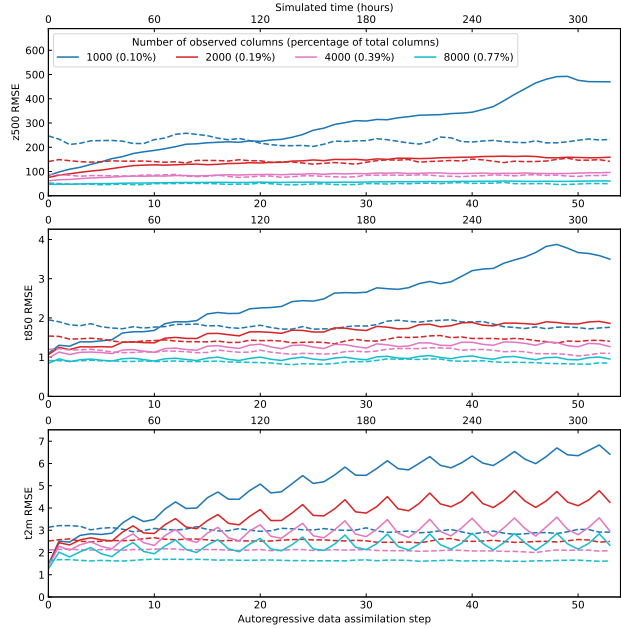


Figure 6. Root mean square errors (RMSEs) of geopotential at 500hPa, temperature at 850hPa and temperature at 2m from autoregressively assimilated data (solid lines) and interpolated observations (dashed lines). The observations are made at the same locations in each assimilation step.

cannot be lower than using ERA5 inputs because the ERA5 data is used to simulate observations in the experiment. However, this setup allows us to compare the forecast errors against ones with longer lead times to determine the extent of lead time lost due to the use of assimilated data as forecast inputs. With 8,000 observed columns, the errors for z_{500} , t_{850} , and t_{2m} are lower than the 72-hour forecast errors. This implies that the lead time lost is less than 24 hours for these variables. With 40,000 observed columns, the error for z_{500} and t_{850} is approximately equivalent to the 60-hour forecast error. However, the t_{2m} errors remain larger than the 60-hour forecast errors, potentially due to diurnal effects that cause a decrease in the forecast errors of t_{2m} from the 48-hour lead time level to a 60-hour lead time level.

3.5. Limitations and future works

Currently, our method can consume point measurements at a single time step as observations (subsection 2.1). This covers weather station and upper-air balloon measurements but does not include satellite imagery and radar soundings which can be represented as functions of the atmospheric states. We are planning to support broader types of observations and multiple time steps using loss-function-based conditioning at the inference period (Chung et al., 2022; Rozet and Louppe, 2023a). In addition, we are going to

DiffDA: a Diffusion model for weather-scale Data Assimilation

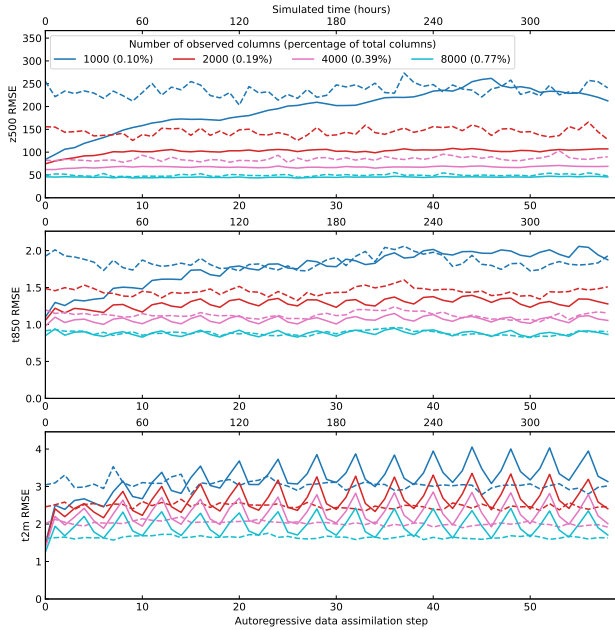


Figure 7. Root mean square errors (RMSEs) of geopotential at 500hPa, temperature at 850hPa and temperature at 2m from autoregressively assimilated data (solid lines) and interpolated observations (dashed lines). The observations are made at different locations in each assimilation step.

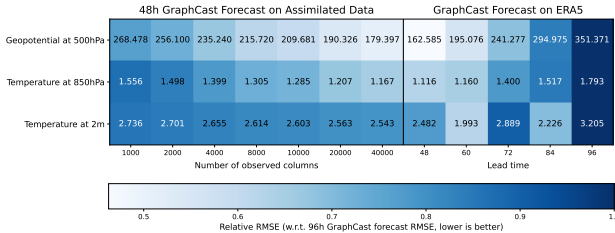


Figure 8. Root mean square errors (RMSEs, shown by the numbers in the cell) of geopotential at 500hPa, temperature at 850hPa, and temperature at 2m from the 48-hour forecast using assimilated data as inputs, and from forecasts with lead times from 48-hour to 96-hour using ERA5 as inputs. The errors are calculated against the ERA5 data. The cells are color-coded with the RMSEs relative to the 96-hour forecast errors.

explore adding conditioning of the satellite imagery directly into the diffusion model similar to the conditioning of the predicted state (subsection 2.3). This requires much more training effort but provides more flexibility as the observation function is learned implicitly. With more input observations, we expect to have more accurate and stable results when performing autoregressive data assimilation.

On the other hand, our method lacks quality control of the input observation data. It takes the input observations as

ground truth values and enforces assimilated data to be consistent with the observations. Therefore, we have to resort to simulated observations from the ERA5 dataset. We are going to investigate possible quality control techniques that either pre-process the data separately or be embedded in the data assimilation process. By addressing the above points, we will achieve a fully operational data assimilation model.

3.6. Conclusion

In summary, we propose a data assimilation method, DiffDA, capable of assimilating high-resolution atmospheric variables up to a horizontal resolution of 0.25° , setting a new record for ML-based data assimilation models. Based on the denoising diffusion model, we adapt the pre-trained GraphCast neural network as the backbone model motivated by its compatible input and output shapes. DiffDA’s flexibility also allows for integrating other forecast models, ensuring easy updates and maintenance. A key feature of DiffDA is the enforcement of conditioning on the predicted state during training and inference periods, and the conditioning of sparse observations exclusively at the inference stage. An additional benefit of this conditioning approach is the automatic generation of a post-processing model, should observations not be supplied at inference time.

The experimental results validated the effectiveness of our method: the assimilated data converges to the observations as the number of observed columns increases. With less than 0.77% of total “real-world” data columns and 48-hour forecast, the error of assimilated data is on par with 24-hour forecast error. When used as an input for forecast models, those assimilated data resulted in a maximum lead time loss of 24 hours compared with using the ERA5 dataset as inputs. This enables running data assimilation and simulation in an autoregressive cycle. It remains a challenge to constrain the errors across the autoregressive iterations. This is likely to be solved by assimilating more real-world observations.

All the data assimilation experiments can run on a single high-end PC with a GPU within 15 - 30 minutes per data assimilation step, while a similar task using traditional methods typically requires large compute clusters. This indicates a significant reduction in computational costs. It also opens up the possibility of assimilating more observational data that is otherwise discarded by traditional methods and producing assimilated data with higher accuracy.

4. Ethical and social impact

This work aims for a more efficient and accurate data assimilation method, which will potentially help reduce the energy costs of weather forecast centers, make better weather forecasts, and provide better data for tackling climate change.

References

- page 35–144. Cambridge University Press, July 2023. ISBN 9781009157896. doi: 10.1017/9781009157896.002. URL <http://dx.doi.org/10.1017/9781009157896.002>.
- G. Andry et al. Data assimilation as simulation-based inference. 2023.
- M. Andrychowicz, L. Espeholt, D. Li, S. Merchant, A. Merose, F. Zyda, S. Agrawal, and N. Kalchbrenner. Deep learning for day forecasts from sparse observations. *arXiv preprint arXiv:2306.06079*, 2023.
- S. Ashkboos, L. Huang, N. Dryden, T. Ben-Nun, P. Dueben, L. Gianinazzi, L. Kummer, and T. Hoefler. Ens-10: A dataset for post-processing ensemble weather forecasts. *Advances in Neural Information Processing Systems*, 35: 21974–21987, 2022.
- R. N. Bannister. A review of operational methods of variational and ensemble-variational data assimilation. *Quarterly Journal of the Royal Meteorological Society*, 143 (703):607–633, 2017.
- K. Bi, L. Xie, H. Zhang, X. Chen, X. Gu, and Q. Tian. Accurate medium-range global weather forecasting with 3d neural networks. *Nature*, 619(7970):533–538, 2023.
- M. Bonavita, E. Hólm, L. Isaksen, and M. Fisher. The evolution of the ecmwf hybrid data assimilation system. *Quarterly Journal of the Royal Meteorological Society*, 142(694):287–303, 2016.
- J. Bradbury, R. Frostig, P. Hawkins, M. J. Johnson, C. Leary, D. Maclaurin, G. Necula, A. Paszke, J. VanderPlas, S. Wanderman-Milne, and Q. Zhang. JAX: composable transformations of Python+NumPy programs, 2018. URL <http://github.com/google/jax>.
- H. Chung, J. Kim, M. T. Mccann, M. L. Klasky, and J. C. Ye. Diffusion posterior sampling for general noisy inverse problems. In *The Eleventh International Conference on Learning Representations*, 2022.
- G. Evensen, F. C. Vossepoel, and P. J. van Leeuwen. *Data assimilation fundamentals: A unified formulation of the state and parameter estimation problem*. Springer Nature, 2022.
- T. S. Finn, L. Disson, A. Farchi, M. Bocquet, and C. Durand. Representation learning with unconditional denoising diffusion models for dynamical systems. *EGU sphere*, 2023: 1–39, 2023.
- H. Hersbach, B. Bell, P. Berrisford, S. Hirahara, A. Horányi, J. Muñoz-Sabater, J. Nicolas, C. Peubey, R. Radu, D. Schepers, et al. The era5 global reanalysis. *Quarterly Journal of the Royal Meteorological Society*, 146 (730):1999–2049, 2020.
- J. Ho, A. Jain, and P. Abbeel. Denoising diffusion probabilistic models. *Advances in neural information processing systems*, 33:6840–6851, 2020.
- R. Lam, A. Sanchez-Gonzalez, M. Willson, P. Wirnsberger, M. Fortunato, F. Alet, S. Ravuri, T. Ewalds, Z. Eaton-Rosen, W. Hu, et al. Learning skillful medium-range global weather forecasting. *Science*, page eadi2336, 2023.
- K. Law, A. Stuart, and K. Zygalakis. Data assimilation. *Cham, Switzerland: Springer*, 214:52, 2015.
- L. Li, R. Carver, I. Lopez-Gomez, F. Sha, and J. Anderson. Seeds: Emulation of weather forecast ensembles with diffusion models. *arXiv preprint arXiv:2306.14066*, 2023.
- I. Loshchilov and F. Hutter. Fixing weight decay regularization in adam. 2018.
- A. Lugmayr, M. Danelljan, A. Romero, F. Yu, R. Timofte, and L. Van Gool. Repaint: Inpainting using denoising diffusion probabilistic models. In *Proceedings of the IEEE/CVF Conference on Computer Vision and Pattern Recognition*, pages 11461–11471, 2022.
- M. Mardani, N. Brenowitz, Y. Cohen, J. Pathak, C.-Y. Chen, C.-C. Liu, A. Vahdat, K. Kashinath, J. Kautz, and M. Pritchard. Generative residual diffusion modeling for km-scale atmospheric downscaling. *arXiv preprint arXiv:2309.15214*, 2023.
- M. Mardani, N. Brenowitz, Y. Cohen, J. Pathak, C.-Y. Chen, C.-C. Liu, A. Vahdat, K. Kashinath, J. Kautz, and M. Pritchard. Residual diffusion modeling for km-scale atmospheric downscaling. 2024.
- J. Pathak, S. Subramanian, P. Harrington, S. Raja, A. Chattopadhyay, M. Mardani, T. Kurth, D. Hall, Z. Li, K. Azizzadenesheli, et al. Fourcastnet: A global data-driven high-resolution weather model using adaptive fourier neural operators. *arXiv preprint arXiv:2202.11214*, 2022.
- I. Price, A. Sanchez-Gonzalez, F. Alet, T. Ewalds, A. El-Kadi, J. Stott, S. Mohamed, P. Battaglia, R. Lam, and M. Willson. Gencast: Diffusion-based ensemble forecasting for medium-range weather. *arXiv preprint arXiv:2312.15796*, 2023.

S. Rasp, P. D. Dueben, S. Scher, J. A. Weyn, S. Mouatadid, and N. Thuerey. Weatherbench: a benchmark data set for data-driven weather forecasting. *Journal of Advances in Modeling Earth Systems*, 12(11):e2020MS002203, 2020.

S. Rasp, S. Hoyer, A. Merose, I. Langmore, P. Battaglia, T. Russel, A. Sanchez-Gonzalez, V. Yang, R. Carver, S. Agrawal, et al. Weatherbench 2: A benchmark for the next generation of data-driven global weather models. *arXiv preprint arXiv:2308.15560*, 2023.

F. Rozet and G. Louppe. Score-based data assimilation. *arXiv preprint arXiv:2306.10574*, 2023a.

F. Rozet and G. Louppe. Score-based data assimilation for a two-layer quasi-geostrophic model. *arXiv preprint arXiv:2310.01853*, 2023b.

C. Saharia, W. Chan, S. Saxena, L. Li, J. Whang, E. L. Denton, K. Ghasemipour, R. Gontijo Lopes, B. Karagol Ayan, T. Salimans, et al. Photorealistic text-to-image diffusion models with deep language understanding. *Advances in Neural Information Processing Systems*, 35:36479–36494, 2022.

Y. Song, J. Sohl-Dickstein, D. P. Kingma, A. Kumar, S. Ermon, and B. Poole. Score-based generative modeling through stochastic differential equations. *arXiv preprint arXiv:2011.13456*, 2020.

P. Virtanen, R. Gommers, T. E. Oliphant, M. Haberland, T. Reddy, D. Cournapeau, E. Burovski, P. Peterson, W. Weckesser, J. Bright, et al. Scipy 1.0: fundamental algorithms for scientific computing in python. *Nature methods*, 17(3):261–272, 2020.

P. von Platen, S. Patil, A. Lozhkov, P. Cuenca, N. Lambert, K. Rasul, M. Davaadorj, and T. Wolf. Diffusers: State-of-the-art diffusion models, 2023. URL <https://github.com/huggingface/diffusers>. Apache-2.0 License.

A. Appendices

A.1. Code Availability

The source code is available in this repository <https://anonymous.4open.science/r/DiffDA-BED0>. The repository includes a modified GraphCast model which has the Apache License version 2.0.

A.2. Scoreboard plots for single-step data assimilation

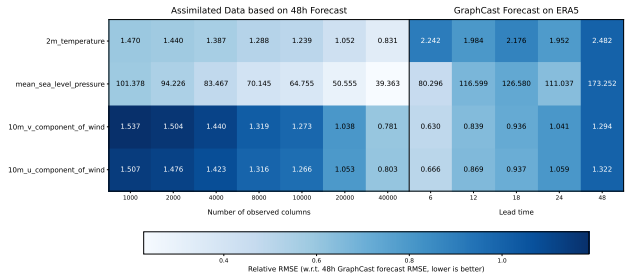


Figure 9. Root mean square errors (RMSEs, shown by the numbers in the cell) of surface variables from the single-step assimilated data, and from 6-hour to 48-hour GraphCast forecasts. The errors are calculated against the ERA5 data. The cells are color-coded with the RMSEs relative to the 48-hour forecast errors.

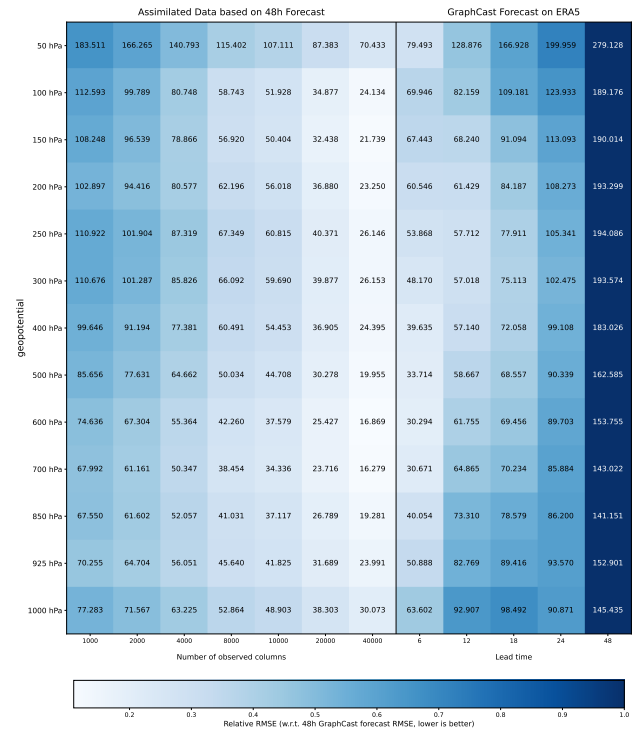


Figure 10. Root mean square errors (RMSEs, shown by the numbers in the cell) of geopotential from the single-step assimilated data, and from 6-hour to 48-hour GraphCast forecasts. The errors are calculated against the ERA5 data. The cells are color-coded with the RMSEs relative to the 48-hour forecast errors.

DiffDA: a Diffusion model for weather-scale Data Assimilation

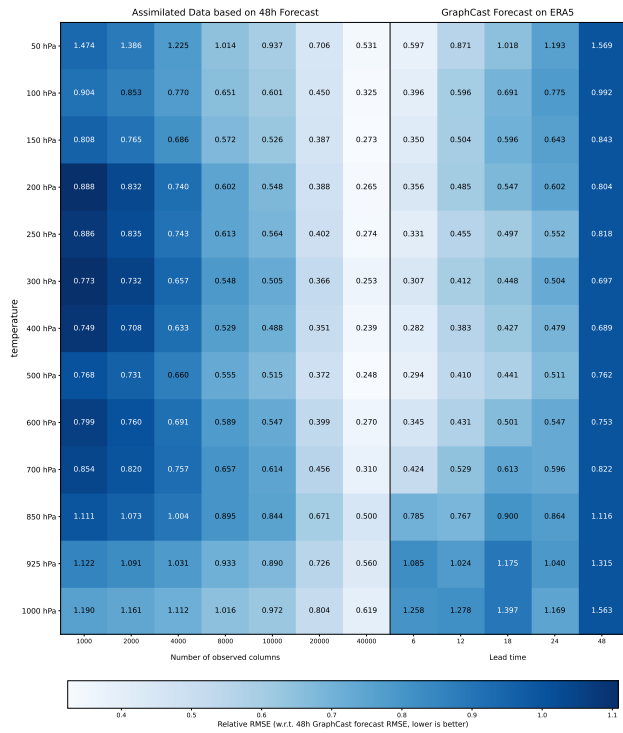


Figure 11. Root mean square errors (RMSEs, shown by the numbers in the cell) of temperature from the single-step assimilated data, and from 6-hour to 48-hour GraphCast forecasts. The errors are calculated against the ERA5 data. The cells are color-coded with the RMSEs relative to the 48-hour forecast errors.

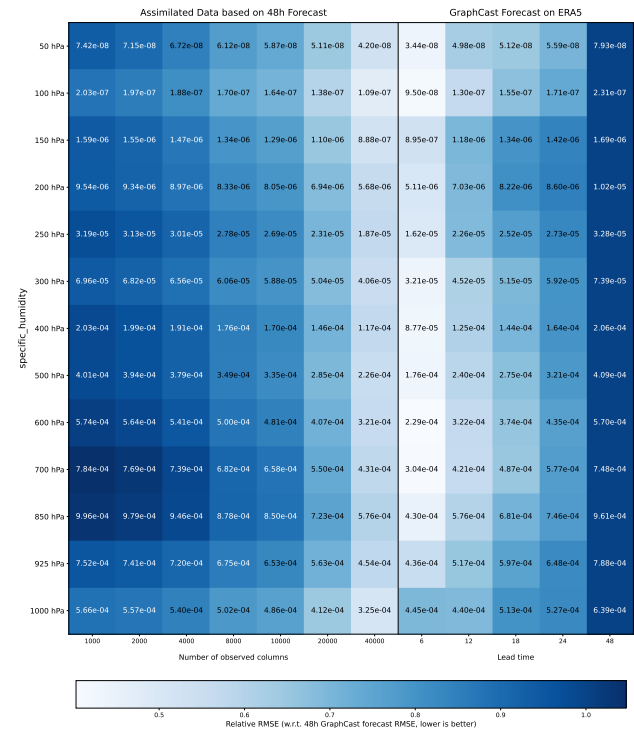


Figure 12. Root mean square errors (RMSEs, shown by the numbers in the cell) of specific humidity from the single-step assimilated data, and from 6-hour to 48-hour GraphCast forecasts. The errors are calculated against the ERA5 data. The cells are color-coded with the RMSEs relative to the 48-hour forecast errors.

DiffDA: a Diffusion model for weather-scale Data Assimilation

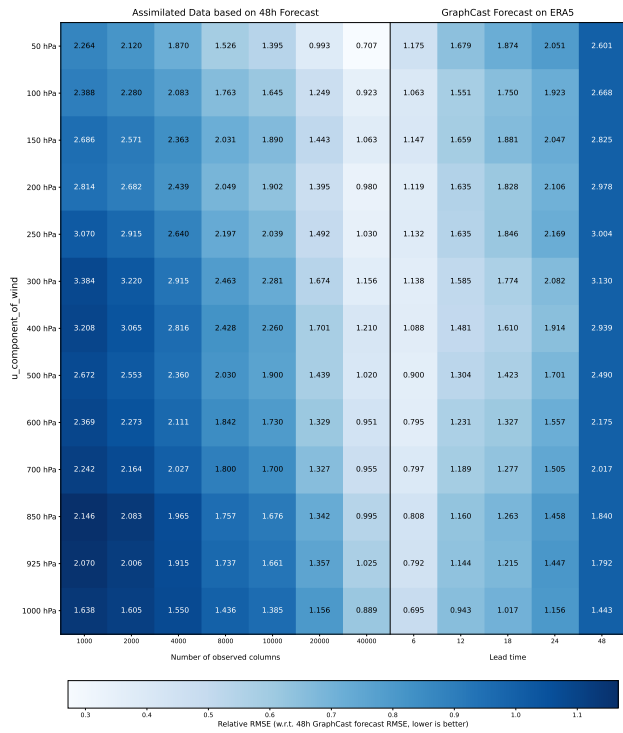


Figure 13. Root mean square errors (RMSEs, shown by the numbers in the cell) of horizontal wind speed (U) from the single-step assimilated data, and from 6-hour to 48-hour GraphCast forecasts. The errors are calculated against the ERA5 data. The cells are color-coded with the RMSEs relative to the 48-hour forecast errors.

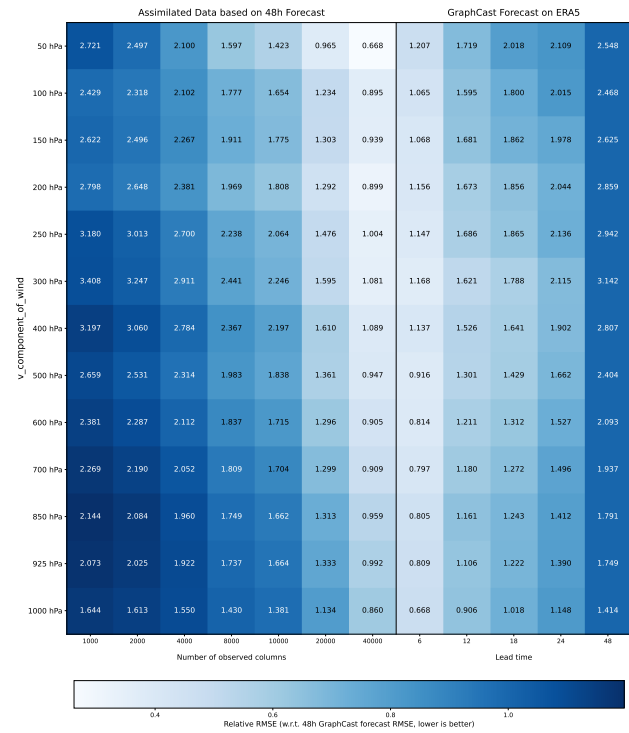


Figure 14. Root mean square errors (RMSEs, shown by the numbers in the cell) of horizontal wind speed (V) from the single-step assimilated data, and from 6-hour to 48-hour GraphCast forecasts. The errors are calculated against the ERA5 data. The cells are color-coded with the RMSEs relative to the 48-hour forecast errors.

DiffDA: a Diffusion model for weather-scale Data Assimilation

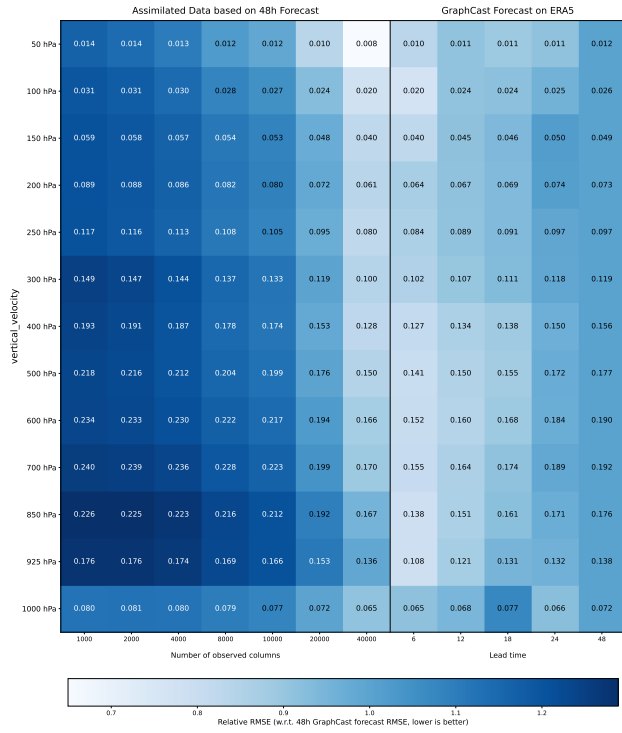


Figure 15. Root mean square errors (RMSEs, shown by the numbers in the cell) of vertical wind speed from the single-step assimilated data, and from 6-hour to 48-hour GraphCast forecasts. The errors are calculated against the ERA5 data. The cells are color-coded with the RMSEs relative to the 48-hour forecast errors.

A.3. Scoreboard plots for forecast on single-step assimilated data

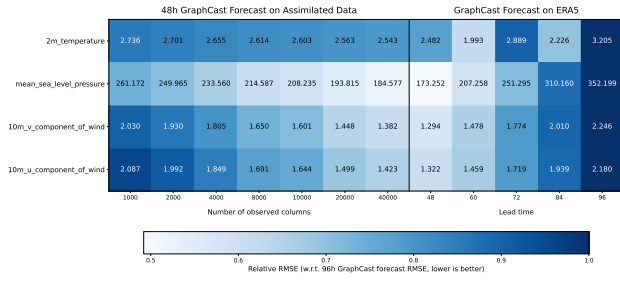


Figure 16. Root mean square errors (RMSEs, shown by the numbers in the cell) of surface variables from the 48-hour forecast using assimilated data as inputs, and from forecasts with lead times from 48-hour to 96-hour using ERA5 as inputs. The errors are calculated against the ERA5 data. The cells are color-coded with the RMSEs relative to the 96-hour forecast errors.

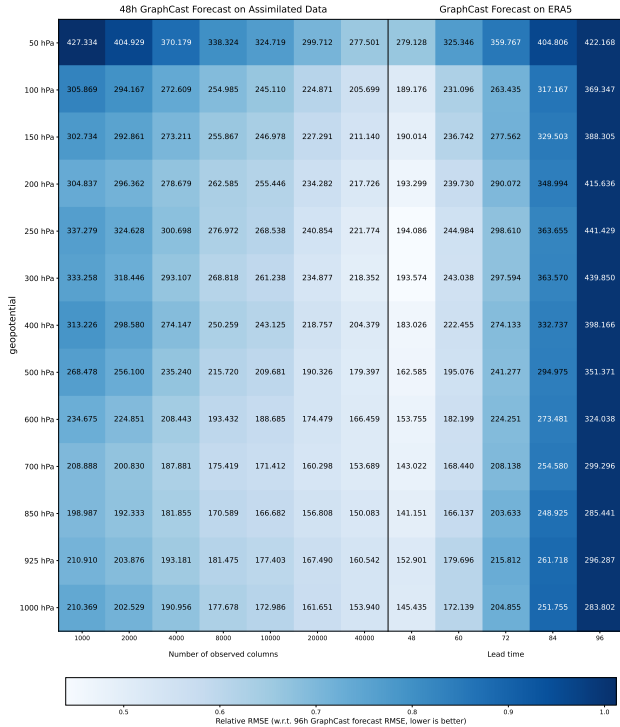


Figure 17. Root mean square errors (RMSEs, shown by the numbers in the cell) of geopotential from the 48-hour forecast using assimilated data as inputs, and from forecasts with lead times from 48-hour to 96-hour using ERA5 as inputs. The errors are calculated against the ERA5 data. The cells are color-coded with the RMSEs relative to the 96-hour forecast errors.

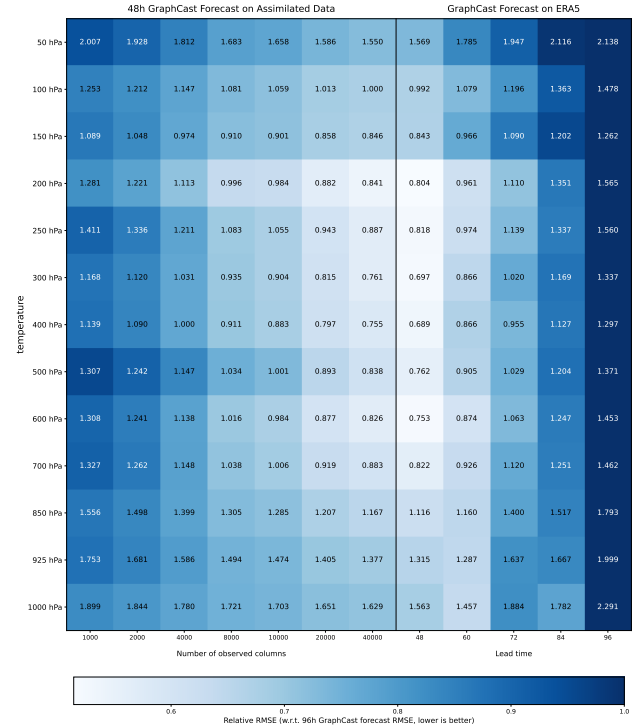


Figure 18. Root mean square errors (RMSEs, shown by the numbers in the cell) of temperature from the 48-hour forecast using assimilated data as inputs, and from forecasts with lead times from 48-hour to 96-hour using ERA5 as inputs. The errors are calculated against the ERA5 data. The cells are color-coded with the RMSEs relative to the 96-hour forecast errors.

DiffDA: a Diffusion model for weather-scale Data Assimilation

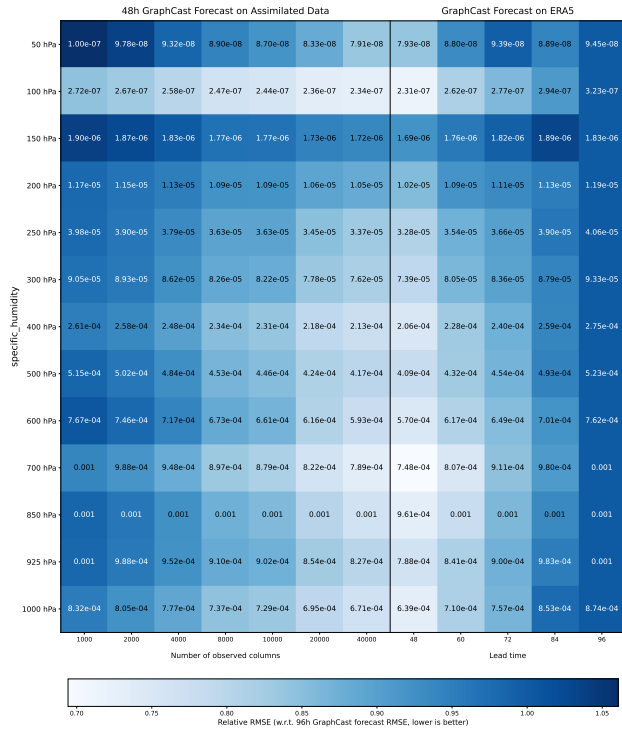


Figure 19. Root mean square errors (RMSEs, shown by the numbers in the cell) of specific humidity from the 48-hour forecast using assimilated data as inputs, and from forecasts with lead times from 48-hour to 96-hour using ERA5 as inputs. The errors are calculated against the ERA5 data. The cells are color-coded with the RMSEs relative to the 96-hour forecast errors.

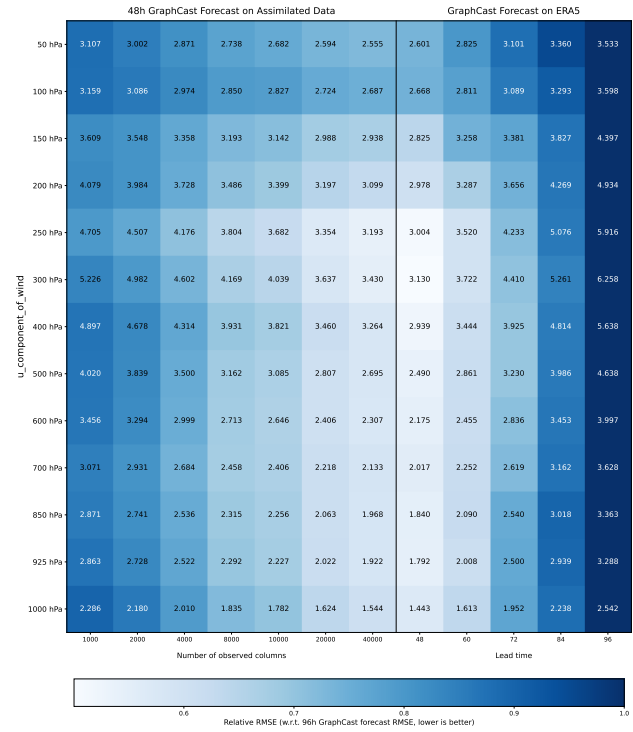


Figure 20. Root mean square errors (RMSEs, shown by the numbers in the cell) of horizontal wind speed (U) from the 48-hour forecast using assimilated data as inputs, and from forecasts with lead times from 48-hour to 96-hour using ERA5 as inputs. The errors are calculated against the ERA5 data. The cells are color-coded with the RMSEs relative to the 96-hour forecast errors.

DiffDA: a Diffusion model for weather-scale Data Assimilation

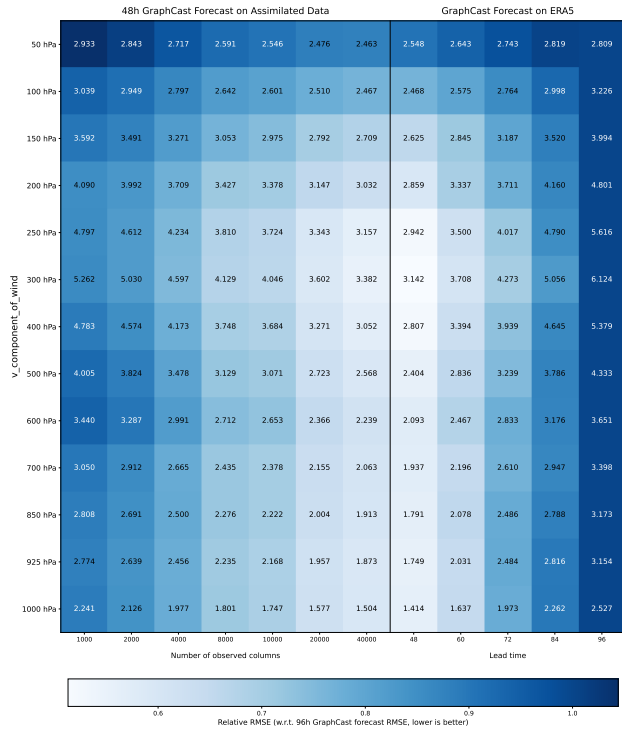


Figure 21. Root mean square errors (RMSEs, shown by the numbers in the cell) of horizontal wind speed (V) from the 48-hour forecast using assimilated data as inputs, and from forecasts with lead times from 48-hour to 96-hour using ERA5 as inputs. The errors are calculated against the ERA5 data. The cells are color-coded with the RMSEs relative to the 96-hour forecast errors.

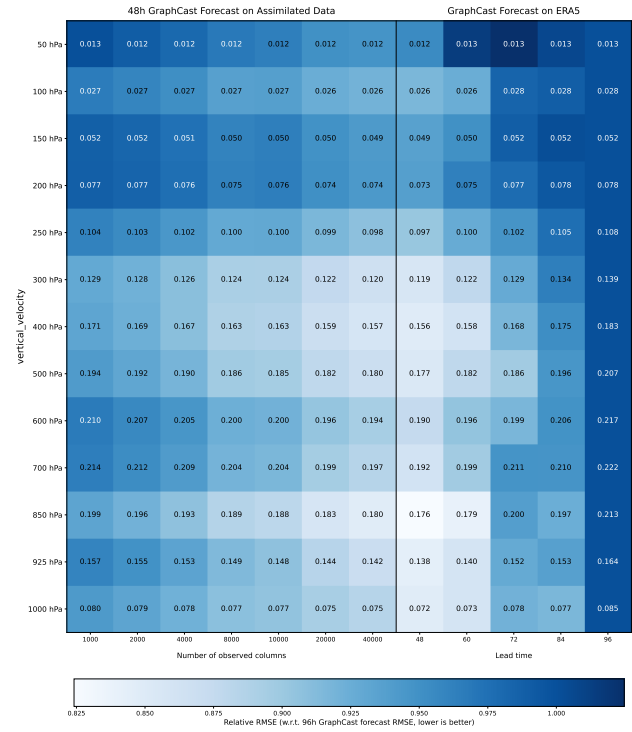


Figure 22. Root mean square errors (RMSEs, shown by the numbers in the cell) of vertical wind speed from the 48-hour forecast using assimilated data as inputs, and from forecasts with lead times from 48-hour to 96-hour using ERA5 as inputs. The errors are calculated against the ERA5 data. The cells are color-coded with the RMSEs relative to the 96-hour forecast errors.